Article

Major southern San Andreas earthquakes modulated by lake-filling events

https://doi.org/10.1038/s41586-023-06058-9

Received: 15 July 2022

Accepted: 5 April 2023

Published online: 7 June 2023

Check for updates

Ryley G. Hill[1,2]✉, Matthew Weingarten[1], Thomas K. Rockwell[1] & Yuri Fialko[2]

Hydrologic loads can stimulate seismicity in the Earth's crust[1]. However, evidence for the triggering of large earthquakes remains elusive. The southern San Andreas Fault (SSAF) in Southern California lies next to the Salton Sea[2], a remnant of ancient Lake Cahuilla that periodically filled and desiccated over the past millennium[3–5]. Here we use new geologic and palaeoseismic data to demonstrate that the past six major earthquakes on the SSAF probably occurred during highstands of Lake Cahuilla[5,6]. To investigate possible causal relationships, we computed time-dependent Coulomb stress changes[7,8] due to variations in the lake level. Using a fully coupled model of a poroelastic crust[9–11] overlying a viscoelastic mantle[12,13], we find that hydrologic loads increased Coulomb stress on the SSAF by several hundred kilopascals and fault-stressing rates by more than a factor of 2, which is probably sufficient for earthquake triggering[7,8]. The destabilizing effects of lake inundation are enhanced by a nonvertical fault dip[14–17], the presence of a fault damage zone[18,19] and lateral pore-pressure diffusion[20,21]. Our model may be applicable to other regions in which hydrologic loading, either natural[8,22] or anthropogenic[1,23], was associated with substantial seismicity.

The SSAF is the only historically quiescent seismogenic section of the San Andreas Fault system (Fig. 1) and is believed to pose the largest seismic hazard in California[14,24,25]. The last major earthquake on the SSAF occurred around 1726 (ref. 26). The modern open interval of about 300 years is well in excess of the average recurrence interval of 180 ± 40 years over the past millennium[4,5,26]. Previous studies suggested that at least some large events on the SSAF may have occurred during highstands of ancient Lake Cahuilla[3,27,28]. Lake Cahuilla was a prehistoric lake that formed from periodic meandering of the Colorado River north into the Salton Trough and had an estimated maximum volume of 236 km^3 (ref. 5). Filling and draining of the lake subjected the SSAF system to surface loads corresponding to a roughly 100-m-deep body of water[3,27,28]. Previous studies suggested that loading owing to ancient Lake Cahuilla inhibited failure on most of the SSAF, except maybe for a small portion within the lake boundary[29], or that triggering of large events on the SSAF was mediated by slip on nearby extensional stepover faults[30]. Here we combine new palaeoseismic and geologic data with state-of-the-art numerical modelling to investigate the relationship between lake loading and major earthquakes on the SSAF over the past approximately 1,100 years.

Palaeoseismic evidence is critically important in determining both the timing of large earthquakes and lake history. Previous work at the Coachella palaeoseismic site, just below the ancient Lake Cahuilla shoreline (Fig. 1), suggested five probable and two possible earthquakes over the past millennium[4]. Recently, Rockwell et al.[6] reinterpreted the stratigraphy at the Coachella site, building on the results developed for the past two full lake inundations, which consider both the historical record and drowned stump ages[5]. Three different lake-level models, varied by different sampling assumptions, were constrained by more than 122 radiocarbon dates across several palaeoseismic sites in the ancient Lake Cahuilla inundation zone. The resulting nearly 2,000-year history of ancient Lake Cahuilla is based on an extensive compilation and review of radiocarbon samples throughout the lake basin and on the unique character of some stratigraphic unit interpretations. Distinct organic layers, measuring 1–2 cm in thickness and originally described as 'soils', were reinterpreted to be the result of lake inundations. These organic-rich layers record where organic materials floated to near the shoreline and were incorporated into a lake sequence during rising lake waters. Supporting this interpretation is the fact that organic soils are not present in the hyper-arid environment of the Lake Cahuilla basin and that such organic layers have been identified only at or below the shoreline of Lake Cahuilla[6,27,31]. Similar observations have also been made along the Laguna Salada Fault further to the south[32].

On the basis of these insights into the palaeolake chronology, we infer that six of the past seven SSAF earthquake horizons lie within lacustrine sediments. This is critical, as new palaeoseismic data that refine the history of lake ages[6] also place tighter constraints on the timing of past earthquakes. We converted the ^{14}C radiocarbon ages of organic material to calendar years CE using the OxCal algorithm v.4.4 and the history of atmospheric ^{14}C concentrations[33,34]. The OxCal algorithm produces probability density functions (PDFs) of each date by convolving uncertainties in the radiocarbon measurements. An ordered sequence based on the stratigraphic layering provides further constraints to the radiocarbon age PDFs. The statistically consistent earthquake PDFs are calculated on the basis of the interpretation of their timings in conjunction with the full sequence. The details of our

[1]Department of Geological Sciences, San Diego State University, San Diego, CA, USA. [2]Scripps Institution of Oceanography, University of California San Diego, La Jolla, CA, USA.
✉e-mail: ryleyghill@gmail.com

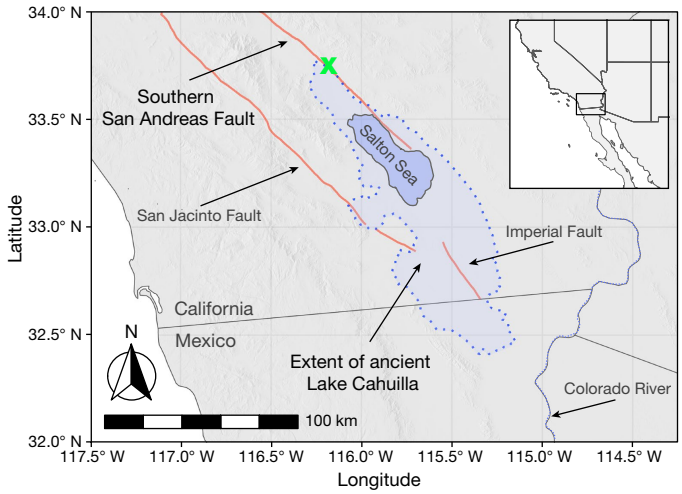

Fig. 1 | Regional context. Map of the Salton Trough and present-day Salton Sea (9.5 m average water depth). Dotted blue line denotes the historical extent of ancient Lake Cahuilla (13 m above sea level; 97.2 m maximum water depth)[29]. Red lines denote traces of several major faults[48]. Green X marks the location of the Coachella palaeoseismic site[4].

interpretation of the palaeoseismic record and OxCal model are provided in the Supplementary Information. Our interpretations of where earthquake horizons lie in the stratigraphy are mostly unchanged from those of Philibosian et al.[4]. The main differences in earthquake ages are a result of reclassifying which sediments are lacustrine, as well as assuming that most charcoal and all organic layers are from material that grew within the lake perimeter, and therefore have ages corresponding to the preceding dry periods between lakes[6]. Figure 2 shows the calculated PDFs for major seismic events that occurred on the SSAF over the past approximately 1,100 years (see Extended Data Table 1 for earthquake dates). Also shown in Fig. 2 is the preferred history model of Lake Cahuilla[6] that includes the following six highstands: 1731–1733 CE (lake A), 1618–1636 CE (lake B), 1486–1503 CE (lake C), 1192–1241 CE (lake D), 1007–1070 CE (lake E) and 930–966 CE (lake F). Highstands are preceded by a 13-year-long inundation period and followed by a 50-year-long dessication period, consistent with previous lake models[5]. The same radiocarbon dates are used to inform the timing of the earthquake and lake ages, but the lake timings are further constrained by climate data[6]. Although previous studies were inconclusive about temporal correlation of the earthquakes and lake episodes over the past millennium[4], the new earthquake history strongly suggests that all lake-filling events were accompanied by large earthquakes (Fig. 2).

Such a correlation between the earthquake and lake timings is probably not coincidental. A Monte Carlo statistical test of the lake and earthquake timings confirms a nonrandom relationship with >97% confidence (Extended Data Fig. 1). Also, hydrologic loads are known to stimulate seismicity[1,23,35–37]. Possible mechanisms include increases in pore pressure, flexural stresses and poroelastic effects[29,30]. Seismicity may be triggered shortly after reservoir impoundment by the poroelastic load of the lake at the Earth's surface, as well as on longer timescales by the time-dependent diffusion of pore pressure to greater depths[1,35,38]. Increases in pore-fluid pressure, in general, bring faults closer to failure and may potentially advance the timing of large events[1,39,40]. Another factor relevant to triggering of seismicity is the presence of fluid pathways resulting from rock damage. Faults are commonly associated with damage zones[18,19], resulting in enhanced permeability that decays with distance away from the fault core[41–45]. Fault damage zones can therefore substantially facilitate fluid transport to seismogenic depths[20,21]. There is evidence for an extensive SSAF damage zone from field observations at surface exposures, borehole data and Earth tidal analyses[46,47]. Models of lake loading therefore need to account for the fully coupled poroelastic response and the heterogeneous hydromechanical properties of the fault zone and ambient crust.

To quantify the effects of lake loading, we built a fully coupled, 3D finite-element model of the Salton Trough that accounts for time-varying surface loads, a realistic fault geometry, crustal poroelasticity and viscoelastic relaxation in the ductile substrate (see Methods and Extended Data Fig. 2). We performed numerical simulations in which we varied material properties of the host rocks and damage zone to constrain a plausible range of pore pressure and stress evolution owing to ancient Lake Cahuilla (Extended Data Fig. 3 and Supplementary Figs. 1–4). The temporal evolution of the lake load, which is ascribed as both pore pressure and vertical stress boundary conditions at the Earth's surface, is constrained by the latest geologic data[6] (Fig. 2). Unless otherwise noted, the models presented below assume the lake depth of 97 m, consistent with previous studies[29], but we also considered a spatially variable surface load controlled by bathymetry. Each lake episode consists of a unique filling, highstand, desiccation and consolidation history. We resolve the coupled deformation transient from the refined approximately 1,100-year lake history with about 200 adaptive time steps across our numerical-model domain. The increase in pore pressure within the basement is highly dependent on the assumed parameters of the fault zone, in particular the damage-zone permeability (Extended Data Table 2). For a given loading history, higher values of permeability give rise to greater pore pressures at depth (Extended Data Fig. 3). Furthermore, similar to the analytic solution (see Methods and Extended Data Fig. 4), we observe the 'memory' effect of pore pressure at depth, whereby subsequent lakes can contribute to higher pore pressure owing to the diffusive time lag of a previous lake superimposing on the next (Fig. 3).

The evolution of faults towards (or away from) failure is commonly described in terms of the Coulomb failure stress (ΔCFS)[7,8,35] (also see Methods). The calculated values of ΔCFS resolved on a potential failure plane (Supplementary Figs. 3 and 6) exhibit a strong sensitivity

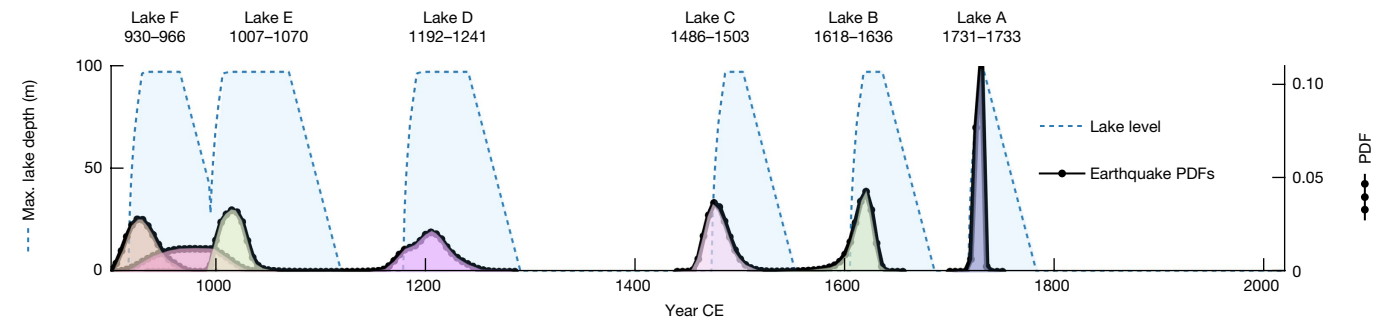

Fig. 2 | Lake and earthquake history. Earthquake PDFs (dotted black lines, right axis) calculated in this study (see Methods) and the relative lake-loading history (dashed blue lines, left axis) from ref. 6. PDFs of prehistoric earthquakes (see Extended Data Table 1) are colour-coded as follows: Coa-1 is blue, Coa-2 is green, Coa-3 and Coa-4 are pink, Coa-5 is magenta, Coa-6 is yellow, Coa-7 is red and Coa-8+ is orange.

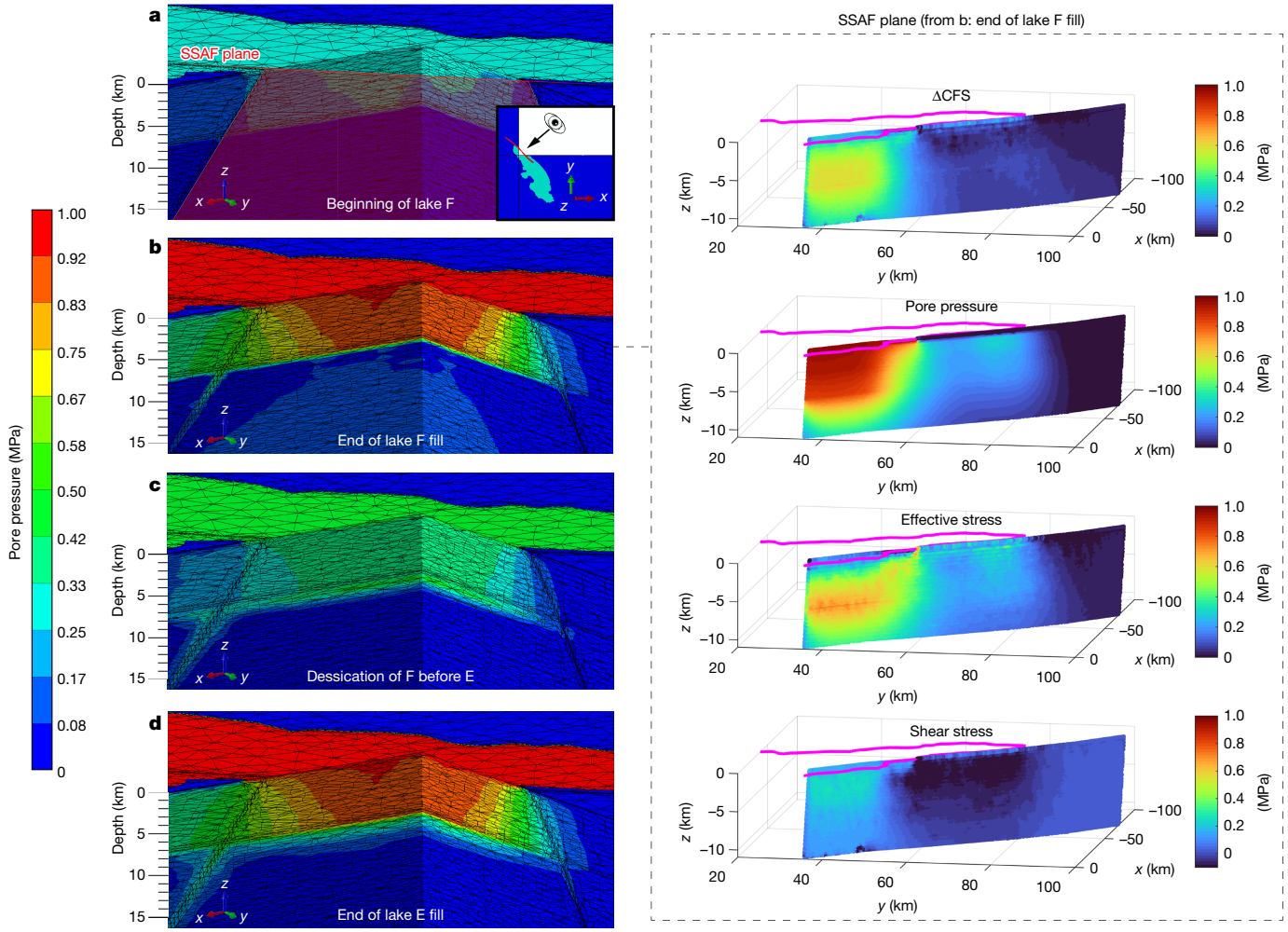

Fig. 3 | Finite-element-model results. Left, spatiotemporal evolution of pore pressure for a single lake cycle of ancient Lake Cahuilla. Calculations assume a constant lake depth of 97.2 m. The cross-section cuts through the northwestern end of the lake and through the embedded dipping fault. **a**, Pore pressure immediately increases as the lake begins to inundate. **b**, At the time of lake highstand, the pore pressure has diffused down much of the higher permeable fault but is more slowly varying elsewhere because of the low-permeability basement. **c**, As the lake desiccates, higher pore pressures remain in and around the fault. **d**, Subsequent lakes further increase the previously elevated pore pressure at basement depth. Right, the Coulomb stress change (ΔCFS), pore pressure (P), effective stress ($\bar{\sigma}_n$) and absolute shear stress (τ_s) perturbations on the SSAF fault plane for a single time frame in the lake cycle. The magenta line represents the outline of ancient Lake Cahuilla at the surface.

to the fault geometry and, in particular, the fault dip angle. We assume an average strike of 313° based on the fault trace[48] (Fig. 1) and a fault dip of 60° NE, which is constrained by geodetic and seismic data[14–16,49]. ΔCFS values are inversely proportional to the fault dip angle: a steeper fault experiences a smaller change in the Coulomb stress and a more shallowly dipping fault experiences a larger change in the Coulomb stress (Supplementary Fig. 1). Another factor affecting ΔCFS is a time-dependent flexure owing to the varying surface load and the associated viscoelastic relaxation in the underlying ductile substrate. For a range of possible substrate viscosities suggested by previous work[29], the effects of viscoelastic relaxation on ΔCFS are relatively minor (Supplementary Fig. 2). Our simulations indicate that variations in the pore pressure are the dominant contributor to the total ΔCFS (Supplementary Figs. 3 and 4). Models that used a simplified representation of only the elastic crust suggested higher values of ΔP but lower values of the effective ΔCFS (Supplementary Figs. 3 and 4).

We find that the magnitude of shear stress ($\Delta\tau_s$), effective normal stress ($\Delta\bar{\sigma}_n$), pore pressure (ΔP) and ΔCFS increase throughout the sequence of flooding cycles (Fig. 4a). Most notably, ΔCFS remains predominantly positive across the fault surface during each cycle (Fig. 4a and Supplementary Videos 1–3). Positive ΔCFS outside the lake boundary, albeit smaller in magnitude, is a consequence of lateral pore-pressure diffusion (Fig. 3 and Supplementary Videos 1–3). When the lake is at highstand, shear stress is positive (that is, encouraging failure) in parts of the fault closest to the lake centre and slightly negative (that is, inhibiting failure) outside the lake. By contrast, the normal stress is negative (that is, inhibiting failure) directly below the lake owing to the increased vertical compression during lake impoundment. However, the effective normal stress stays positive on much of the fault because of increases in pore pressure. The modelled compression directly below the lake simply moderates the magnitude of the Coulomb stress in that region. Models with lower permeability show a similar evolution, although the spatial extent of pore-pressure diffusion is smaller.

Figure 4 depicts the evolution of ΔCFS for a single point on the fault plane near the centre of the lake at the representative seismogenic depth of 7 km (point 21 in Supplementary Fig. 5) for a range of models (models 1–5; see Extended Data Table 2) with different permeabilities of the fault damage zone[15,30]. In each model, as the lake fills, the ΔCFS increases rapidly owing to the initial lake impoundment (that is, undrained response). During the desiccation phase of the lakes, the overall ΔCFS decreases but remains mostly positive except for the

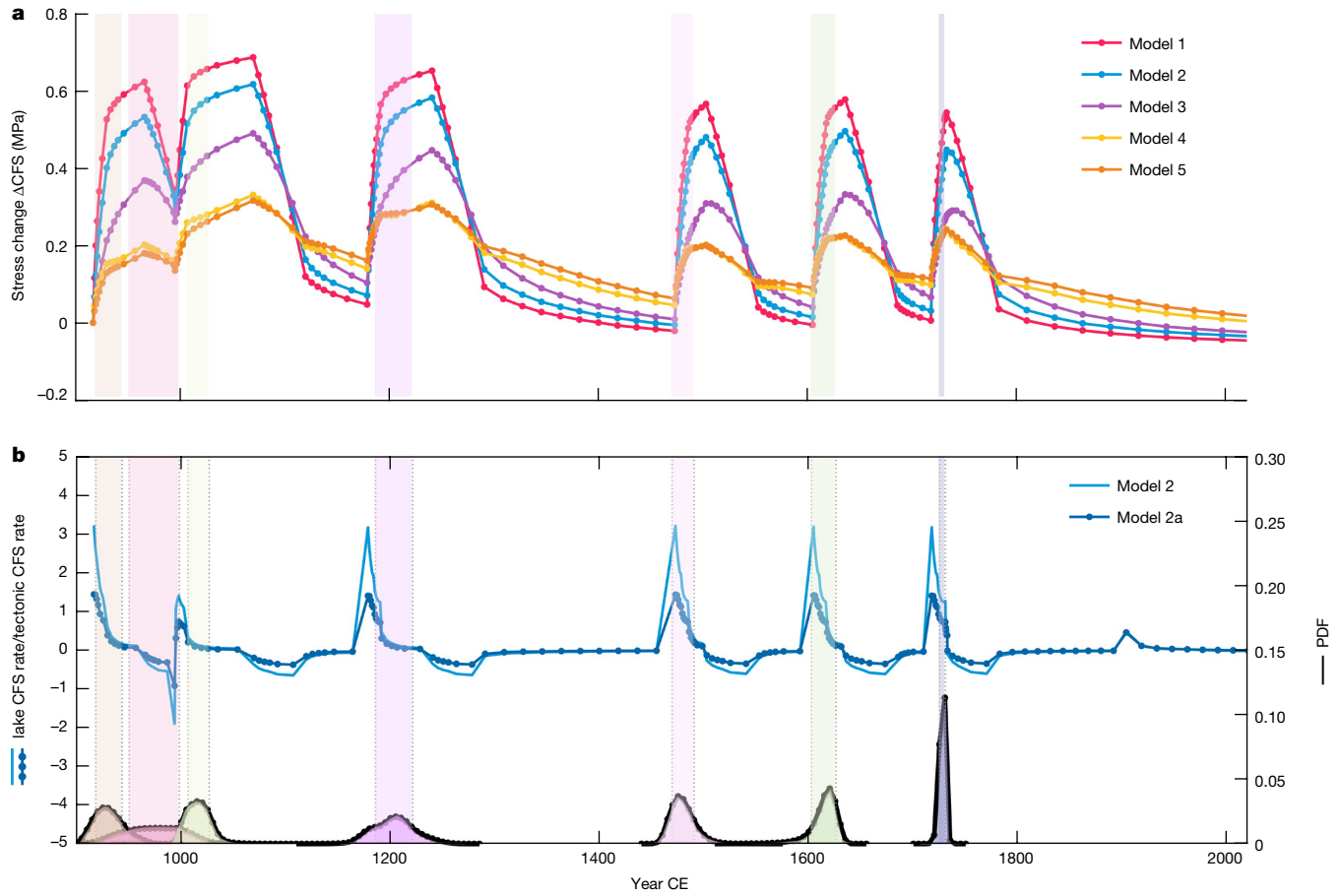

Fig. 4 | Stress effects of lake loading. a, ΔCFS (MPa) on the SSAF as a function of time (year CE) at 7 km depth for location 21, a point on the fault near the centre of the lake (see Supplementary Fig. 5). Coloured lines correspond to models assuming different permeability of the fault zone (see Methods and Extended Data Table 2), from highest (model 1) to lowest (model 5, no permeability contrast with the host rocks). The same plot for a point farther from the lake centre also shows predominantly positive ΔCFS, albeit of lower magnitude (Extended Data Fig. 5). **b**, The Coulomb stressing rate owing to the lake loading normalized by the tectonic loading rate (16 kPa year^{-1}; see Methods). Light blue line represents predictions of model 2 (same as in panel **a**) and dark blue dotted line represents predictions of model 2a, which considers a spatially variable surface load based on a local bathymetry. The small peak in 1905 is because of the inundation of the Salton Sea (see Supplementary Figs. 5–11). Models 1–5 do not include Salton Sea inundation. Vertical colour bars denote ±2 standard deviations of the estimated earthquake dates.

current dry period from about 1733 to the present and the dry period between lakes C and D. The models at the high end of the assumed damage stay positive in most parts of the fault-zone permeability, showing a relatively rapid diffusion of pore pressure from the surface to seismogenic depths. The increased rate of ΔCFS during the lake highstands is indicative of the higher permeability. Furthermore, the results depict how the short time interval between highstands in the first two or three lakes contributes to an overall cumulative increase in the Coulomb stress for the second (lake E) and sometimes the third (lake D) lakes, depending on the modelled fault permeability and depth. The remnant diffusion of pore pressure because of the first lake (lake F) coincides with the impoundment of the subsequent lake, producing a larger overall ΔCFS. This additive effect is even more pronounced for lower fault-zone permeabilities. We acknowledge that shorter lake highstands would reduce the additive effect on ΔCFS discussed in this paper, as we use the maximum durations for the lake highstands[6]. We also performed simulations in which the surface load is controlled by a local bathymetry. The results are similar to the reference model assuming a constant depth of 97 m, except that the calculated stress changes and stressing rates are reduced by around 40%. This is because the average lake depth is less than the maximum depth of 97 m. Predictions of the reference model therefore should be considered an upper bound. Depending on the rate of diffusion, depth of interest and time interval between lakes, the effect of previous lakes may persist during subsequent impoundments. This memory effect is more pronounced for models 3 and 4 owing to lower permeability at depth (Extended Data Fig. 5). All models, including model 5, which does not include a fault damage zone, produce positive ΔCFS values greater than about 0.1 MPa, which is probably large enough for earthquake triggering[7,50,51].

As well as the magnitude of stress changes, earthquake triggering may be affected by variations in the stressing rate[52,53]. We evaluate the ratio of the calculated stressing rate from the lake load to the average tectonic loading rate over time (Fig. 4b). The latter is calculated using a geodetically constrained dislocation model assuming a secular slip rate of 18 mm year^{-1} (ref. 54), which is in agreement with the most recent constraints on the long-term geologic slip rate[55] (and references therein). The estimated tectonic stressing rate at seismogenic depth is $\dot{\sigma}_{13}$ = 16 kPa year^{-1} (see Methods). We find that the largest perturbations in stressing rates occur, as expected, during the early flooding stages of each of the past six lakes (Fig. 4b). For six of the past seven earthquake events on the SSAF (±2σ uncertainties; Extended Data Table 1), the resolved stressing rate from lake loading was greater than the tectonic loading rate. The respective perturbations remain positive through the lake highstands until dessication begins, during which the stressing rates drop below the average interseismic stressing rate. Over

the past approximately 1,100 years, the fault-stressing rate during lake loading increased by more than a factor of 2 (Fig. 4b). These high stressing rates from lake loading persisted for several decades during each lake cycle. The relationship between lake cycles and earthquakes is potentially known at higher precision exclusively from the stratigraphy. There is evidence to suggest that events Coa-5 and Coa-8+ may have occurred during lake-filling phases, whereas Coa-1, Coa-2, Coa-3 and Coa-4, and Coa-6 occurred during highstands (see Methods).

Loading from ancient Lake Cahuilla induced stress changes capable of triggering events on the SSAF, increased ΔCFS across most of the fault and, on average, increased peak stressing rates during lake flooding well above the tectonic stressing rate (Fig. 4b and Supplementary Videos 1–3). Larger fault locking depths[17] and smaller earthquake nucleation depths[56] and elastic moduli of the host rocks[57] would result in a lower tectonic stressing rate and a correspondingly higher contribution of the lake loading. Our model does not account for possible memory effects from earthquakes that occurred more than about 1,000 years ago, as such effects are probably negligible if the interseismic interval exceeds several hundred years (see Fig. 4a; also see ref. 58). We also do not account for stress transfer resulting from slip on subsidiary faults that could potentially amount to ΔCFS on the order of 1 MPa (ref. 30). Our models thus provide a conservative estimate for the modulation of stress on the SSAF by the filling and desiccation of ancient Lake Cahuilla.

Our results bear on the current 300-year-long quiescent period on the SSAF. Variations in stress and stressing rate on the SSAF owing to the lake load suggest that a gradual decline in water level since ancient Lake Cahuilla's last highstand may affect the timing of the SSAF's next event. Indeed, our model predicts predominantly negative ΔCFS for sufficiently long dry periods. The negative ΔCFS during dry periods is primarily because of the flexure of the upper crust caused by a decreased lake level and, to a lesser degree, viscoelastic relaxation below the brittle–ductile transition. A gradual decrease in the ΔCFS since the last highstand was briefly reversed in 1905–1907 because of an overflow of the Colorado River into Salton Basin, which led to formation of the present-day Salton Sea[30]. Our model predicts a sharp increase in ΔCFS, on the order of 0.1 MPa, for most of the fault during the filling phase of the Salton Sea from 1905 to 1907 (Supplementary Figs. 5–11). This increase in ΔCFS was accompanied by the 18 April 1906 M_l 6.1 (MMI 8) event in the Salton Trough near Brawley, CA. This event was previously argued to be triggered by the great 1906 California earthquake near San Francisco that occurred 11 h before and 700 km away from the M_l 6.1 event[59]. It is possible that such distant triggering was facilitated by the lake load. After 1907, the model predicts a subsequent decrease in ΔCFS as the Salton Sea started to decline below the 0.1 MPa triggering threshold (Supplementary Figs. 5–11 and Supplementary Videos 1–3). Further desiccation of the Salton Sea in the future will continue to have a stabilizing effect on the SSAF, but potentially increase the stress to be released in a future event (or a sequence of events).

Our results demonstrate how improved palaeoseismic and palaeolake records, together with advanced models of hydrologic loading of a heterogeneous poroelastic crust, provide new insights into the relationship between water-level variations of ancient Lake Cahuilla and the past seven major earthquakes on the SSAF. We find that increases in lake level result in positive Coulomb stress changes on most of the SSAF, with stressing rates as high as two to three times the tectonic loading rate. Positive ΔCFS values are also seen on sections of the SSAF that are outside the lake owing to lateral diffusion of pore pressure along a permeable fault zone. This indicates that our model predictions are not strongly sensitive to uncertainties in the location of nucleation sites of past (as well as future) large events on the SSAF (see Supplementary Figs. 5–11 and Supplementary Videos 1–3). The pore-pressure 'memory effect' amplifies the contribution of successive lakes provided that intervals between inundations do not substantially exceed the characteristic diffusion time within the seismogenic layer. Our model may also be applicable to other areas in which seismogenic faults are subject to hydrologic loads from natural or anthropogenic sources[1,22,37].

Online content

Any methods, additional references, Nature Portfolio reporting summaries, source data, extended data, supplementary information, acknowledgements, peer review information; details of author contributions and competing interests; and statements of data and code availability are available at https://doi.org/10.1038/s41586-023-06058-9.

1. Talwani, P. On the nature of reservoir-induced seismicity. *Pure Appl. Geophys.* **150**, 473–492 (1997).
2. Tostrud, M. B. *The Salton Sea, 1906-1996, Computed and Measured Salinities and Water Levels*. Draft Report, Colorado River Board of California (1997).
3. Waters, M. R. Late Holocene lacustrine chronology and archaeology of ancient Lake Cahuilla, California. *Quat. Res.* **19**, 373–387 (1983).
4. Philibosian, B., Fumal, T. & Weldon, R. San Andreas fault earthquake chronology and Lake Cahuilla history at Coachella, California. *Bull. Seismol. Soc. Am.* **101**, 13–38 (2011).
5. Rockwell, T. K., Meltzner, A. J. & Haaker, E. C. Dates of the two most recent surface ruptures on the southernmost San Andreas fault recalculated by precise dating of Lake Cahuilla dry periods. *Bull. Seismol. Soc. Am.* **108**, 2634–2649 (2018).
6. Rockwell, T. K., Meltzner, A. J., Haaker, E. C. & Madugo, D. The late Holocene history of Lake Cahuilla: two thousand years of repeated fillings within the Salton Trough, Imperial Valley, California. *Quat. Sci. Rev.* **282**, 107456 (2022).
7. King, G. C. P., Stein, R. S. & Lin, J. Static stress changes and the triggering of earthquakes. *Bull. Seismol. Soc. Am.* **84**, 935–953 (1994).
8. Cocco, M. Pore pressure and poroelasticity effects in Coulomb stress analysis of earthquake interactions. *J. Geophys. Res. Solid Earth* **107**, 2030 (2002).
9. Rice, J. R. & Cleary, M. P. Some basic stress diffusion solutions for fluid-saturated elastic porous media with compressible constituents. *Rev. Geophys.* **14**, 227–241 (1976).
10. Wang, H. *Theory of Linear Poroelasticity: With Applications to Geomechanics and Hydrogeology* (Princeton Univ. Press, 2000).
11. LaBonte, A., Brown, K. & Fialko, Y. Hydrogeologic detection and finite-element modeling of a slow slip event in the Costa Rica prism toe. *J. Geophys. Res. Solid Earth* **114**, B00A02 (2009).
12. Segall, P. *Earthquake and Volcano Deformation* (Princeton Univ. Press, 2010).
13. Barbot, S. & Fialko, Y. A unified continuum representation of post-seismic relaxation mechanisms: semi-analytic models of afterslip, poroelastic rebound and viscoelastic flow. *Geophys. J. Int.* **182**, 1124–1140 (2010).
14. Fialko, Y. Interseismic strain accumulation and the earthquake potential on the southern San Andreas fault system. *Nature* **441**, 968–971 (2006).
15. Lin, G., Shearer, P. M. & Hauksson, E. Applying a three-dimensional velocity model, waveform cross correlation, and cluster analysis to locate southern California seismicity from 1981 to 2005. *J. Geophys. Res. Solid Earth* **112**, B12309 (2007).
16. Fuis, G. S., Scheirer, D. S., Langenheim, V. E. & Kohler, M. D. A new perspective on the geometry of the San Andreas fault in Southern California and its relationship to lithospheric structure. *Bull. Seismol. Soc. Am.* **102**, 236–251 (2012).
17. Lindsey, E. O. et al. Interseismic strain localization in the San Jacinto fault zone. *Pure Appl. Geophys.* **171**, 2937–2954 (2014).
18. Fialko, Y. et al. Deformation on nearby faults induced by the 1999 Hector Mine earthquake. *Science* **297**, 1858–1862 (2002).
19. Cochran, E. S. et al. Seismic and geodetic evidence for extensive, long-lived fault damage zones. *Geology* **37**, 315–318 (2009).
20. Caine, J. S., Evans, J. P. & Forster, C. B. Fault zone architecture and permeability structure. *Geology* **24**, 1025–1028 (1996).
21. Bense, V., Gleeson, T., Loveless, S., Bour, O. & Scibek, J. Fault zone hydrogeology. *Earth Sci. Rev.* **127**, 171–192 (2013).
22. Nof, R. et al. Rising of the lowest place on Earth due to Dead Sea water-level drop: evidence from SAR interferometry and GPS. *J. Geophys. Res. Solid Earth* **117**, B05412 (2012).
23. Gupta, H. K. *Reservoir Induced Earthquakes* (Elsevier, 1992).
24. Weldon, R. J., Fumal, T. E., Biasi, G. P. & Scharer, K. M. Past and future earthquakes on the San Andreas fault. *Science* **308**, 966–967 (2005).
25. Field, E. H. et al. Uniform California Earthquake Rupture Forecast, version 3 (UCERF3)—the time-independent model. *Bull. Seismol. Soc. Am.* **104**, 1122–1180 (2014).
26. Fumal, T. E. Timing of large earthquakes since AD 800 on the Mission Creek strand of the San Andreas fault zone at Thousand Palms Oasis, near Palm Springs, California. *Bull. Seismol. Soc. Am.* **92**, 2841–2860 (2002).
27. Gurrola, L. D. & Rockwell, T. K. Timing and slip for prehistoric earthquakes on the Superstition Mountain fault, Imperial Valley, southern California. *J. Geophys. Res. Solid Earth* **101**, 5977–5985 (1996).
28. Thomas, A. P. & Rockwell, T. K. A 300- to 550-year history of slip on the Imperial fault near the U.S.-Mexico border: missing slip at the Imperial fault bottleneck. *J. Geophys. Res. Solid Earth* **101**, 5987–5997 (1996).
29. Luttrell, K., Sandwell, D., Smith-Konter, B., Bills, B. & Bock, Y. Modulation of the earthquake cycle at the southern San Andreas fault by lake loading. *J. Geophys. Res. Solid Earth* **112**, B08411 (2007).
30. Brothers, D., Kilb, D., Luttrell, K., Driscoll, N. & Kent, G. Loading of the San Andreas fault by flood-induced rupture of faults beneath the Salton Sea. *Nat. Geosci.* **4**, 486–492 (2011).

31. Sieh, K. Slip rate across the San Andreas fault and prehistoric earthquakes at Indio, California. *Eos Trans. AGU* **67**, 1200 (1986).
32. Mueller, K. *Neotectonics, Alluvial History and Soil Chronology of the Southwestern Margin of the Sierra de Los Cucapas, Baja California Norte*. Master's thesis, San Diego State Univ. (1984).
33. Bronk Ramsey, C. Bayesian analysis of radiocarbon dates. *Radiocarbon* **51**, 337–360 (2009).
34. Reimer, P. J. et al. The IntCal20 Northern Hemisphere radiocarbon age calibration curve (0–55 cal kBP). *Radiocarbon* **62**, 725–757 (2020).
35. Roeloffs, E. Fault stability changes induced beneath a reservoir with cyclic variations in water level. *J. Geophys. Res. Solid Earth* **93**, 2107–2124 (1988).
36. Segall, P. Earthquakes triggered by fluid extraction. *Geology* **17**, 942–946 (1989).
37. Gupta, H. K. A review of recent studies of triggered earthquakes by artificial water reservoirs with special emphasis on earthquakes in Koyna, India. *Earth Sci. Rev.* **58**, 279–310 (2002).
38. Rajendran, K. & Talwani, P. The role of elastic, undrained, and drained responses in triggering earthquakes at Monticello Reservoir, South Carolina. *Bull. Seismol. Soc. Am.* **82**, 1867–1888 (1992).
39. Simpson, D., Leith, W. & Scholz, C. Two types of reservoir-induced seismicity. *Bull. Seismol. Soc. Am.* **78**, 2025–2040 (1988).
40. Tao, W., Masterlark, T., Shen, Z. & Ronchin, E. Impoundment of the Zipingpu reservoir and triggering of the 2008 M_w 7.9 Wenchuan earthquake, China. *J. Geophys. Res. Solid Earth* **120**, 7033–7047 (2015).
41. Mitchell, T. & Faulkner, D. The nature and origin of off-fault damage surrounding strike-slip fault zones with a wide range of displacements: a field study from the Atacama fault system, northern Chile. *J. Struct. Geol.* **31**, 802–816 (2009).
42. Dor, O., Ben-Zion, Y., Rockwell, T. & Brune, J. Pulverized rocks in the Mojave section of the San Andreas Fault Zone. *Earth Planet. Sci. Lett.* **245**, 642–654 (2006).
43. Rockwell, T. et al. Chemical and physical characteristics of pulverized Tejon Lookout granite adjacent to the San Andreas and Garlock faults: implications for earthquake physics. *Pure Appl. Geophys.* **166**, 1725–1746 (2009).
44. Morton, N., Girty, G. H. & Rockwell, T. K. Fault zone architecture of the San Jacinto fault zone in Horse Canyon, southern California: a model for focused post-seismic fluid flow and heat transfer in the shallow crust. *Earth Planet. Sci. Lett.* **329**, 71–83 (2012).
45. Rempe, M. et al. Damage and seismic velocity structure of pulverized rocks near the San Andreas Fault. *J. Geophys. Res. Solid Earth* **118**, 2813–2831 (2013).
46. Morrow, C., Lockner, D., Moore, D. & Hickman, S. Deep permeability of the San Andreas fault from San Andreas fault observatory at depth (SAFOD) core samples. *J. Struct. Geol.* **64**, 99–114 (2014).
47. Xue, L., Brodsky, E. E., Erskine, J., Fulton, P. M. & Carter, R. A permeability and compliance contrast measured hydrogeologically on the San Andreas Fault. *Geochem. Geophys. Geosyst.* **17**, 858–871 (2016).
48. USGS and California Geological Survey. *Quaternary Fault and Fold Database for the United States* (accessed 10 July 2019); https://www.usgs.gov/natural-hazards/earthquake-hazards/faults/.
49. Schulte Pelkum, V., Ross, Z. E., Mueller, K. & Ben Zion, Y. Tectonic inheritance with dipping faults and deformation fabric in the brittle and ductile southern California crust. *J. Geophys. Res. Solid Earth* **125**, e2020JB019525 (2020).
50. Goebel, T., Weingarten, M., Chen, X., Haffener, J. & Brodsky, E. The 2016 Mw5.1 Fairview, Oklahoma earthquakes: Evidence for long-range poroelastic triggering at >40 km from fluid disposal wells. *Earth Planet. Sci. Lett.* **472**, 50–61 (2017).
51. Verdecchia, A., Cochran, E. S. & Harrington, R. M. Fluid-earthquake and earthquake-earthquake interactions in Southern Kansas, USA. *J. Geophys. Res. Solid Earth* **126**, e2020JB020384 (2021).
52. Toda, S., Stein, R. S. & Sagiya, T. Evidence from the AD 2000 Izu islands earthquake swarm that stressing rate governs seismicity. *Nature* **419**, 58–61 (2002).
53. Qin, Y., Chen, T., Ma, X. & Chen, X. Forecasting induced seismicity in Oklahoma using machine learning methods. *Sci. Rep.* **12**, 9319 (2022).
54. Lindsey, E. & Fialko, Y. Geodetic slip rates in the southern San Andreas Fault system: effects of elastic heterogeneity and fault geometry. *J. Geophys. Res. Solid Earth* **118**, 689–697 (2013).
55. Blanton, C. M., Rockwell, T. K., Gontz, A. & Kelly, J. T. Refining the spatial and temporal signatures of creep and co-seismic slip along the southern San Andreas Fault using very high resolution UAS imagery and SfM-derived topography, Coachella Valley, California. *Geomorphology* **357**, 107064 (2020).
56. Jin, Z. & Fialko, Y. Finite slip models of the 2019 Ridgecrest earthquake sequence constrained by space geodetic data and aftershock locations. *Bull. Seismol. Soc. Am.* **110**, 1660–1679 (2020).
57. Eissa, E. & Kazi, A. Relation between static and dynamic Young's moduli of rocks. *Int. J. Rock Mech. Min. Geomech. Abstr.* **25**, 479–482 (1988).
58. Salditch, L. et al. Earthquake supercycles and long-term fault memory. *Tectonophysics* **774**, 228289 (2020).
59. Meltzner, A. J. & Wald, D. J. Aftershocks and triggered events of the great 1906 California earthquake. *Bull. Seismol. Soc. Am.* **93**, 2160–2186 (2003).

Methods

Calculation of the Coulomb stress changes

The change in ΔCFS is defined as[7,8,35]:

$$\Delta \mathrm{CFS} = \Delta\tau_s + \mu(\Delta\sigma_n + \Delta P) \quad (1)$$

in which $\Delta\tau_s$ is the change in shear stress, μ is the coefficient of friction, $\Delta\sigma_n$ is the change in normal stress (increases in compression are deemed negative) and ΔP is the change in pore-fluid pressure (increases in fluid pressure are deemed positive). The sign convention indicates that a positive change in the effective stress $\overline{\sigma_n} = \sigma_n + P$, as well as a positive change in shear stress $\Delta\tau_s$, promote failure. In this paper, we assume a typical value for static friction of $\mu = 0.6$ (refs. 60–63), although it may vary considerably depending on the rock type and ambient conditions[64–66]. The Coulomb stress changes ΔCFS are computed by resolving the normal and absolute shear-stress components using a full stress tensor, the prescribed fault geometry and sense of slip. Calculations were performed using the MATLAB toolbox Abaqus2Matlab[67].

Both the magnitude and the sign of the estimated ΔCFS is sensitive to several parameters in the context of poroelastic deformation, including: (1) the fault-zone permeability, width and connectivity to regions in which large seismic events nucleate. Higher permeability values allow for pore pressure to diffuse faster, increasing pore pressure and ΔCFS at depth[68,69]. A larger fault zone width and pore connectivity may also increase pore pressure and ΔCFS on the fault at greater depths[70]. (2) The fault dip angle[14,16], the varying geometry of the lake and the concomitant surface load[29]. The lake load produces regions of relative compression and extension within the seismogenic crust (Extended Data Fig. 6). Regardless of the fault attitude and sense of slip, increases in the fault-normal compressive stress are expected to inhibit failure and decreases in compressive stress are expected to promote failure. (3) The undrained pore-pressure effect, without which the total pore pressure will be underestimated[40,71] (Extended Data Fig. 6).

Fully coupled 3D finite-element models

The governing equations for a fully coupled linear poroelastic 3D medium are defined as[9,10,72]:

$$G\nabla^2 u_i + \frac{G}{1-2\nu}\frac{\partial^2 u_j}{\partial x_i \partial x_j} = \alpha\frac{\partial P}{\partial x_i} - F_i \quad (2)$$

$$\alpha\frac{\partial \epsilon_{ii}}{\partial t} + S_\epsilon\frac{\partial P}{\partial t} = \frac{k}{\mu}\nabla^2 P + Q \quad (3)$$

in which G is the shear modulus, u the displacement, υ the Poisson's ratio, α the Biot–Willis coefficient, F the body force, k the permeability, μ the fluid viscosity, S_ϵ the constrained specific storage, ϵ_{ii} the dilatancy (trace of the strain tensor), P the pore pressure and Q the fluid source[10]. Equations (2) and (3) are nearly identical to the classic equations for linear elasticity and diffusion of pore pressure, except for the coupling of pore pressure in the conservation of momentum equation (2) and the fluid flow coupled to strain by the requirement of fluid continuity equation (3). Analytic solutions to the system in equations (2) and (3) are restricted to a few highly idealized cases. We solve the respective equations numerically using the 3D finite-element software Abaqus SIMULIA[11,73].

As a preliminary cross-check, we considered a 1D analytic solution for a periodic fluctuation of a surface load in a poroelastic half-space[35] (see Methods). For a reasonable choice of model parameters, the analytic solution shows a cumulative increase in pore pressure at depth through several inundation events. This 'memory effect' is because of the fact that the maximum pore-pressure increase at depth is delayed owing to diffusion and does not completely vanish before the next flooding event. The timing of the superposition depends on the depth, permeability and wavelength of the lake load. One important caveat is that the memory effect only emerges when one considers several lake cycles.

To account for spatial heterogeneity and anisotropy of the hydraulic properties of the lake sediments, upper crust and the fault zone, we construct a 3D hydromechanical model based on parameters constrained by previous studies. Tompson et al.[74] developed and arranged the hydrostratigraphy of the Salton Trough sediments into three broad classes in order of increasing depth: Brawley, Palm Spring and Imperial formations. The composition of these formations vary from sandstones to shales, shaley sandstones, conglomeratic and arkosic sandstones (see Extended Data Table 2). The Salton Trough sediments directly overlie a basement formation and upper mantle layer. The elastic parameters of the basement formation are based on inference from seismic-wave velocities and hydrological parameters are based on crustal-depth dependencies, which produce material properties close to those of Westerly granite[10,75,76] (Extended Data Table 2). A crustal thickness of 18 km is assumed on the basis of seismic observations of the region[77]. We modelled the upper mantle both as an elastic (Supplementary Figs. 6 and 7) and a viscoelastic layer. The viscoelastic mantle is modelled similarly to previous studies as a simple linear Maxwell material[29,78–80]. We use a nonlinear geometry option in Abaqus (NLGEOM) based on the results of Hampel et al.[81], who recommended it for models involving isostatic effects[81].

The fault damage zone is modelled in accordance with field hydrogeologic estimates of San Andreas Fault permeability[47]. Xue et al.[47] estimated a relatively high permeability (10^{-14} m^2) constrained by borehole tidal responses using Earth tidal analysis compared with inferred permeability in the region and laboratory values[46,82,83]. We use this estimate of permeability as a high-end value and explore a range of fault-damage-zone permeabilities between the high-end value and permeability of the ambient crust (that is, no contrast in permeability between the fault-zone material and the host rocks; Extended Data Table 2). Therefore, we test the sensitivity of our model results to a range of fault permeabilities from $k = 10^{-14}$ m^2 (model 1) to values consistent with the intact crystalline basement $k = 10^{-18}$ m^2 (model 5)[76]. The fault permeability in model 1 is considered high when compared with other fault zones worldwide or laboratory measurements. Thus, our preferred model (model 2) uses $k = 10^{-15}$ m^2, which is more consistent with regional measurements and laboratory data[46,82,83]. Observations also show that the effective shear modulus of rocks within a fault zone may be lower than that of the host rock by as much as a factor of 2 (refs. 17–19,84). In our model, the shear modulus of rocks in the fault zone is taken to be a factor of 2 smaller than the shear modulus of the host rocks (Extended Data Table 2).

The numerical domain was developed and discretized in Abaqus CAE[73]. The numerical domain has horizontal dimensions 600 km × 600 km and a depth of 50 km, with the y axis corresponding to north for the Universal Transverse Mercator 11N zone (Extended Data Fig. 2). The finite-element mesh consists of nearly 2 million first-order linear tetrahedral elements. Characteristic element sizes vary from 30,000 m in the far field to less than 100 m on the fault and lake edges. The SSAF fault trace is based on the USGS Quaternary fault database[48]. We model a 60° northeast dip for the SSAF, which is consistent with geodetic slip models, seismicity and seismic tomography data[49,54]. We consider a 200-m-wide damage zone centred on the SSAF slip interface[19,46,84]. The lake shoreline is based on coordinates used by Luttrell et al.[29] and a similar assumption in lake depth (97.2 m) across the entire lake footprint to maintain consistency in model comparisons[5,29]. Models that considered spatially variable lake depth used the SRTM digital elevation model[85] and bathymetry of the Salton Sea to assign the vertical stress and pressure boundary conditions at the nodes within the lake boundaries.

The evolution of the poroelastic effects requires a careful consideration of the model boundary and initial conditions. We assume initial

conditions of equilibrium stress and pore pressure (chapter 9 in ref. 12). These conditions imply that the model only considers the effect of the lake and does not include any loading from tectonic stress. Gravity is included, with stress and pore pressure calculated as relative change from geostatic equilibrium. This is an important consideration, as neglecting gravity in the viscoelastic model may overestimate surface displacements on timescales that exceed the characteristic relaxation time[13,86]. The bottom and sides of the model are fixed in the surface-normal direction and free of shear stress (a 'roller' condition). The bottom of the poroelastic domain is considered to be insulated (zero-flux boundary condition), whereas the sides and top of the model are considered to be permeable and subject to vanishing pore pressure ($P = 0$). The top surface of the model is stress-free outside the lake area. The lake extent is the only boundary condition that varies over time.

Tectonic loading

We approximate the secular tectonic loading using a model of a screw dislocation in an elastic half-space[87] (see equation (2.25) in ref. 12). The respective interseismic shear strain rate is given by:

$$\dot{\epsilon}_{13} = \frac{-\dot{s}}{4\pi}\left[\frac{x_2 - d_2}{(x_2 - d_2)^2 + x_1^2} - \frac{x_2 + d_2}{(x_2 + d_2)^2 + x_1^2}\right] \quad (4)$$

in which $\dot{s}$ is the fault slip rate (taken to be 18 mm year^{-1} (ref. 54)), x_1 is the horizontal coordinate with respect to the centre of the fault damage zone, x_2 is the assumed depth of nucleation of large events and $d = 10$ km is the estimated locking depth of the SSAF[54,88].

For typical values of the shear modulus of the upper crust $G = 28–32$ GPa (ref. 54), the stressing rate predicted by equation (4) at the bottom of the seismogenic zone ($x_2 = 6–8$ km) is $\dot{\sigma}_{13} = 2G(\dot{\epsilon}_{13}) = 25 - 51$ kPa year^{-1}. However, the distribution of stressing rates throughout the seismogenic layer depends on details of a transition between the locked and creeping parts of the fault (for example, ref. 89), as well as the degree of strain localization below the brittle–ductile transition (for example, ref. 90). A dislocation model overpredicts the stressing rate, especially at the bottom of the seismogenic zone, owing to a strong stress singularity. Also, the depth distribution of earthquakes in California shows that most earthquakes nucleate at depths of 3–4 km (ref. 56). Therefore, we use the stressing rate at the free surface ($x_2 = 0$), $\dot{\sigma}_{13} \approx 16$ kPa year^{-1}, as a conservative lower bound for the entire seismogenic layer.

San Andreas Fault, Coachella site earthquake history

The Coachella palaeoseismic site (33.72722° N, 116.16976° W) trenches provide evidence of six or seven lake phases and five to seven earthquakes on the SSAF over the past millenium[6]. Four types of stratigraphy have been identified at the Coachella site: lake clay/silt, recessional sand, aeolian sand and fluvial alluvium. The distinction between aeolian sand and recessional sand may be difficult, as the aeolian sand can be derived entirely from the recessional and shoreline sand deposits. See Fig. 5 in Philibosian et al.[4] for a generalized view of the stratigraphic section and brief descriptions of each unit.

An 'organic-rich layer' is described near the top of unit 1L, which is markedly similar to other organic mats from near-shoreline sites that are interpreted as the debris that accumulates near the shoreline from the inundation of the lake basin. Unit 1L is described as a massive silt layer of lacustrine origin. An alternative interpretation is that unit 1L represents deltaic sedimentation during flooding of the site. In either case, 1L and 1S collectively represent regional lake A at the Coachella site[6] (see their supplementary materials). The most recent event occurred during the highstand of Lake Cahuilla in 1726 ± 7 CE (refs. 5,31).

The penultimate lake earthquake, Coa-2, clearly occurs during deposition of unit 2L, which represents the lacustrine phase of lake B, based on extensive liquefaction (only possible with water present) and upward fault terminations[4,6]. That places Coa-2 to have occurred during lake B.

Coa-3 was interpreted to have occurred during lake C based on weak evidence of sediment (unit 3L) filling a structural trough. Coa-4 was interpreted as occurring before lake C but between two organic layers in unit 4S. However, the reinterpretation is that these organic layers were deposited during the rising stages of lake C along with fine sand deposits (probably of deltaic origin), implying that Coa-4 occurred during the early phase of lake C and that the structural trough formed by Coa-4 was filled by the same lake phase, lake C (ref. 6). Belle Philibosian agrees with this reinterpretation (Rockwell, personal communication, 2022). This means that the evidence for Coa-3 and Coa-4 are the same and that there was only one rupture, which occurred during the filling phase of lake C, but when the water had essentially reached the highstand shoreline (as the Coachella site lies at 9 m, only 4 m below the highstand).

Coa-5 was interpreted by Philibosian et al. as having occurred between the deposition of units 5S and 4L, with the units 5S and 5L folded and capped by undeformed unit 4L (ref. 4). Rockwell et al. interpret the organic unit at the top of unit 5S to represent the inundation and accumulation of organics associated with the drowning phase of lake D (ref. 6). Coa-5 deforms the organic layer along with the underlying lake deposits, implying that the earthquake occurred after its deposition during the rising stages of lake D. Supporting this interpretation, the strata of units 5L and 5S are plastically deformed, which—in this arid environment—almost certainly required the presence of water, which will only be present during a lake stand. Hence, Coa-5 is interpreted to have occurred during lake D and probably during the late filling stage, as the event is capped by fine-grained deposition associated with the highstand of lake D.

Coa-6 is interpreted to have occurred during deposition of unit 5L (lake E) based on apparent upward terminations and a possible colluvial wedge of material derived from unit 5L. This evidence was considered weak, but the presented images look convincing, so we confirm the occurrence of a rupture during the highstand of lake E.

Event Coa-7 is interpreted to have occurred between units 6S and 5L based on upward terminations and displaced strata capped by undeformed strata. This would potentially place this earthquake to between lakes E and F, as there is no evidence of the presence of water at that time (no documented liquefaction).

A seventh event, Coa8+, is interpreted to have occurred in unit 7S, which Philibosian et al. describe as "coarse sand, gravel, and rounded cobbles form cross-cutting channel deposits", which are obviously fluvial in origin[4]. Unit 7L is bedded fine sand and is only exposed at the very base of the section. It is interpreted by Philibosian et al. as 'likely lacustrine' but a lake affiliation is not clearly demonstrated. An alternative interpretation is that unit 7L is a deltaic section that was buried by a large fluvial flood event (not a lake-filling flood event) during rising lake level. The rationale for this is that unit 7S is several metres thick and dating a charcoal sample from unit 7S returned an age of 1185 ± 30 RCYBP (radiocarbon years before present; sample Sb4m14A-c), which is consistent with lake F or the dry period immediately preceding lake F and not the much older lake G.

Furthermore, the unit does not show the oxidation that is characteristic for sediments of unit G, which were exposed at the surface for nearly a thousand years. Hence, we interpret the charcoal date as indicating that 7L may actually be the lower part of lake F (deltaic rising lake phase). If correct, an earthquake occurred during the early depositional phase of lake F, followed by a large depositional event and then more lacustrine sediments. The well-sorted sand of the base of unit 7S seems to extend down through unit 7L and may represent a feeder pipe, with the lowest part of unit 7S possibly a liquefaction deposit.

Periodic loading of a poroelastic half-space

As a preliminary, we consider an analytical solution for a periodic fluctuation of water level over a poroelastic half-space[35]. For a half-space extending in the positive direction of the z (vertical) axis from $z = 0$ to $z = \infty$ with a periodic water load of amplitude p_s at the surface given as both vertical stress and pore-pressure boundary conditions $\sigma_{zz}(z = 0, t) = -p(z = 0, t) = p_s \exp(iwt)$ leads to the following solution[10]:

$$\bar{p}_z = \gamma p_s + (1 - \gamma) p_s \exp\left(-z\sqrt{(w/2c)}\right) \exp\left(-\mathrm{i}z\sqrt{(w/2c)}\right) \quad (5)$$

in which $\gamma = \frac{B(1+\upsilon_u)}{3(1-\upsilon_u)}$ is the loading efficiency and c is the diffusivity. If we assume incompressible grains and fluid ($\gamma = 1$), then the response is entirely the vertical stress associated with water load and constant at all depths (undrained response) (Extended Data Fig. 6). The other endmember ($\gamma = 0$) assumes that the pore pressure is uncoupled from the applied stress and is given by the pore-pressure-diffusion solution (drained response)[10,91] (equation (5)) (Extended Data Fig. 6). Moreover, equation (5) is linear with respect to p_s. If $p(0, t)$ is known, the solution for $p(z, t)$ may be parameterized in the frequency domain with the Green's function that carries a pressure disturbance for frequency w at $z = 0$ to $z > 0$:

$$p(z, t) = \int G(z, w) H(w) \mathrm{e}^{-\mathrm{i}wt} \mathrm{d}w \quad (6)$$

in which

$$G(z, w) = \gamma + (1 - \gamma) \exp\left(-z\sqrt{w/2c}\right) \exp\left(-\mathrm{i}z\sqrt{w/2c}\right)$$

and $H(w)$ is the Fourier transform of the surface ($z = 0$) history of the pressure:

$$p(0, t) = \int H(w) \mathrm{e}^{-\mathrm{i}wt} \mathrm{d}w$$

Therefore, if we know the lake-loading history at the surface, $p(0, t)$, we can simply take its Fourier transform, multiply this pore-pressure distribution with the Green's function (equation (6)) in the frequency domain and take the inverse Fourier transform of the product to arrive at the solution to the pore-pressure distribution for all depths and times (Extended Data Fig. 4).

Given a quasi-periodic lake-loading history[6], the distribution of pore pressure shows an interesting effect. Although the shape of the pore-pressure distribution beyond the Earth's surface is entirely dependent on the poroelastic constants in equation (5), for reasonable values of poroelastic constants of rocks comprising the upper crust (Extended Data Table 2), the high frequency of the surface lake levels show a gradual increase of pore-pressure magnitude. This effect would not be present in a 'single-lake' simulation, as the amplitude of the maximum P would just decay exponentially. Instead, with several lakes, the 'memory' pore-pressure effect is the result of a superposition of each independent Fourier component of $p(0, t)$. For example, the diffusive (drained) component of the poroelastic response of lake F (Supplementary Fig. 5) lags its surface response at depth. This is readily observed at greater depth (9 km), at which essentially only the instantaneous (undrained) response to the surface load is felt through the entire load of a single lake cycle. Consequently, the lag of the maximum (drained) response of pore pressure can coincide with the maximum (undrained) response of pore pressure for subsequent lakes, thus leading to larger pore pressures compared with a single-lake response. Therefore, with several lakes, there is an inherent temporal dependence of the maximum pore pressure. A point in our finite-element model (model 2) below the lake at a depth of 7.2 km that lies within our fault is more coincident to the 1D model at shallower 1 km depth (Extended Data Fig. 5). This 1D solution serves to conceptualize the important delayed memory effects of variable pore pressure. Although the analytical 1D solution is a useful first-order approximation, especially for locations directly below the lake, it fails to account for other potentially important factors affecting stress on the fault, such as crustal heterogeneities, viscoelastic relaxation and lateral pore-fluid diffusion.

Data availability

The Abaqus data files, Lake Cahuilla and Salton Sea data files and processed model results are available on Zenodo (http://doi.org/10.5281/zenodo.7714217). Source data are provided with this paper.

Code availability

All relevant MATLAB post-processing codes and sample-plotting codes are available on Zenodo (http://doi.org/10.5281/zenodo.7714217).

60. Byerlee, J. Friction of rock. *Pure Appl. Geophys.* **116**, 615–626 (1978).
61. Sibson, R. H. An assessment of field evidence for 'Byerlee' friction. *Pure Appl. Geophys.* **142**, 645–662 (1994).
62. Fialko, Y. & Jin, Z. Simple shear origin of the cross-faults ruptured in the 2019 Ridgecrest earthquake sequence. *Nat. Geosci.* **14**, 513–518 (2021).
63. Fialko, Y. Estimation of absolute stress in the hypocentral region of the 2019 Ridgecrest, California, earthquakes. *J. Geophys. Res. Solid Earth* **126**, e2021JB022000 (2021).
64. Lockner, D. A., Morrow, C., Moore, D. & Hickman, S. Low strength of deep San Andreas fault gouge from SAFOD core. *Nature* **472**, 82–85 (2011).
65. Mitchell, E., Fialko, Y. & Brown, K. M. Temperature dependence of frictional healing of Westerly granite: experimental observations and numerical simulations. *Geochem. Geophys. Geosyst.* **14**, 567–582 (2013).
66. Mitchell, E., Fialko, Y. & Brown, K. Frictional properties of gabbro at conditions corresponding to slow slip events in subduction zones. *Geochem. Geophys. Geosyst.* **16**, 4006–4020 (2015).
67. Papazafeiropoulos, G., Muñiz-Calvente, M. & Martínez-Pañeda, E. Abaqus2Matlab: a suitable tool for finite element post-processing. *Adv. Eng. Softw.* **105**, 9–16 (2017).
68. Durham, W. B. Laboratory observations of the hydraulic behavior of a permeable fracture from 3800 m depth in the KTB pilot hole. *J. Geophys. Res. Solid Earth* **102**, 18405–18416 (1997).
69. Miller, S. A. The role of fluids in tectonic and earthquake processes. *Adv. Geophys.* **54**, 1–46 (2013).
70. Chang, K. W. & Segall, P. Injection-induced seismicity on basement faults including poroelastic stressing. *J. Geophys. Res. Solid Earth* **121**, 2708–2726 (2016).
71. Ge, S. Comment on "Evidence that the 2008 Mw 7.9 Wenchuan earthquake could not have been induced by the Zipingpu Reservoir" by Kai Deng, Shiyong Zhou, Rui Wang, Russell Robinson, Cuiping Zhao, and Wanzheng Cheng. *Bull. Seismol. Soc. Am.* **101**, 3117–3118 (2011).
72. Biot, M. A. General theory of three dimensional consolidation. *J. Appl. Phys.* **12**, 155–164 (1941).
73. Dassault Systèmes. *Abaqus 2019* (Dassault Systèmes, 2019, 2020).
74. Tompson, A. et al. *Groundwater Availability Within the Salton Sea Basin Final Report* (Lawrence Livermore National Laboratory, 2008).
75. Allam, A. A. & Ben-Zion, Y. Seismic velocity structures in the southern California plate-boundary environment from double-difference tomography. *Geophys. J. Int.* **190**, 1181–1196 (2012).
76. Shmonov, V., Vitiovtova, V., Zharikov, A. & Grafchikov, A. Permeability of the continental crust: implications of experimental data. *J. Geochem. Explor.* **78-79**, 697–699 (2003).
77. Richards-Dinger, K. B. & Shearer, P. M. Estimating crustal thickness in southern California by stacking *PmP* arrivals. *J. Geophys. Res. Solid Earth* **102**, 15211–15224 (1997).
78. Lundgren, P. E., Hetland, A., Liu, Z. & Fielding, E. J. Southern San Andreas-San Jacinto fault system slip rates estimated from earthquake cycle models constrained by GPS and interferometric synthetic aperture radar observations. *J. Geophys. Res. Solid Earth* **114**, B02403 (2009).
79. Pearse, J. & Fialko, Y. Mechanics of active magmatic intraplating in the Rio Grande Rift near Socorro, New Mexico. *J. Geophys. Res. Solid Earth* **115**, B07413 (2010).
80. Johnson, K. Slip rates and off-fault deformation in Southern California inferred from GPS data and models. *J. Geophys. Res. Solid Earth* **118**, 5643–5664 (2013).
81. Hampel, A., Lüke, J., Krause, T. & Hetzel, R. Finite-element modelling of glacial isostatic adjustment (GIA): use of elastic foundations at material boundaries versus the geometrically non-linear formulation. *Comput. Geosci.* **122**, 1–14 (2019).
82. Brace, W. F. Permeability of crystalline and argillaceous rocks. *Int. J. Rock Mech. Min. Sci. Geomech. Abstr.* **17**, 241–251 (1980).
83. Ross, Z. E., Cochran, E. S., Trugman, D. T. & Smith, J. D. 3D fault architecture controls the dynamism of earthquake swarms. *Science* **368**, 1357–1361 (2020).
84. Jeppson, T. N., Bradbury, K. K. & Evans, J. P. Geophysical properties within the San Andreas Fault Zone at the San Andreas Fault Observatory at Depth and their relationships to rock properties and fault zone structure. *J. Geophys. Res. Solid Earth* **115**, B12423 (2010).
85. Farr, T. & Kobrick, M. Shuttle Radar Topography Mission produces a wealth of data. *Eos* **81**, 583–585 (2000).
86. Pollitz, F. F. & Sacks, I. S. The 1995 Kobe, Japan, earthquake: a long-delayed aftershock of the offshore 1944 Tonankai and 1946 Nankaido earthquakes. *Bull. Seismol. Soc. Am.* **87**, 1–10 (1997).
87. Savage, J. & Burford, R. Geodetic determination of relative plate motion in central California. *J. Geophys. Res.* **78**, 832–845 (1973).

88. Lin, G., Shearer, P. M. & Hauksson, E. Applying a three-dimensional velocity model, waveform cross correlation, and cluster analysis to locate southern California seismicity from 1981 to 2005. *J. Geophys. Res. Solid Earth* **112**, B12309 (2007).
89. Lindsey, E. O. & Fialko, Y. Geodetic constraints on frictional properties and earthquake hazard in the Imperial Valley, Southern California. *J. Geophys. Res. Solid Earth* **121**, 1097–1113 (2016).
90. Takeuchi, C. & Fialko, Y. Dynamic models of interseismic deformation and stress transfer from plate motion to continental transform faults. *J. Geophys. Res. Solid Earth* **117**, B05403 (2012).
91. Turcotte, D. L. & Schubert, G. *Geodynamics* 2nd edn (Cambridge Univ. Press, 2002).

Acknowledgements This work was supported by the Southern California Earthquake Center (grant 21091) to M.W. and NSF (EAR-1841273), NASA (80NSSC22K0506) and USGS (G20AP00051) to Y.F. This research benefited from correspondence with R. Guyer. This project used Quaternary fault data from the USGS. We acknowledge use of the CSRC high-performance computing cluster at San Diego State University.

Author contributions R.G.H. constructed the finite-element model, performed analysis of the model results and wrote the manuscript. M.W. managed the study, assisted with building the model, provided access to the modelling software, acquired funding, helped conceive the experiment and commented on the manuscript. T.K.R. carried out the palaeoseismic analysis, conceived the experiment and contributed to the manuscript. Y.F. provided advice on modelling and interpretation of the model results and contributed to the manuscript.

Competing interests The authors declare no competing interests.

Additional information

Supplementary information The online version contains supplementary material available at https://doi.org/10.1038/s41586-023-06058-9.

Correspondence and requests for materials should be addressed to Ryley G. Hill.

Peer review information *Nature* thanks the anonymous reviewers for their contribution to the peer review of this work. Peer reviewer reports are available.

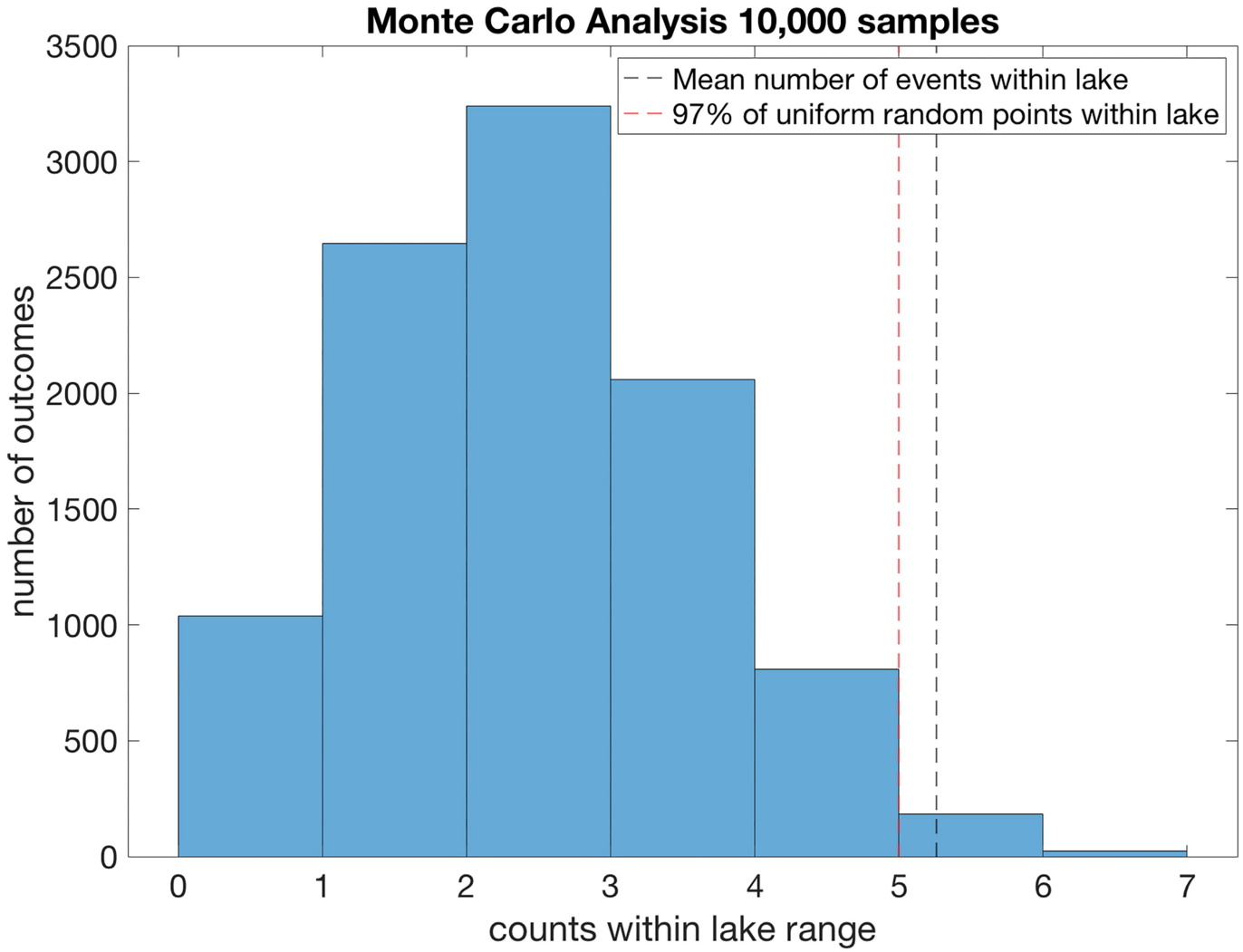

Extended Data Fig. 1 | Monte Carlo statistical test of the lake and earthquake timings. Results of Monte Carlo statistical testing (10,000 samples) based on sampling earthquake PDF distributions and lake timings. After sampling the earthquake PDFs, we determine how many fall inside the lake timings when the lake was greater than 70% full. We compare these timings to a uniform random distribution of seven times across the same lake-loading-time range. We find that the mean timings that occur within lakes is >97% of the earthquake timings of a uniform random distribution that occur within lakes.

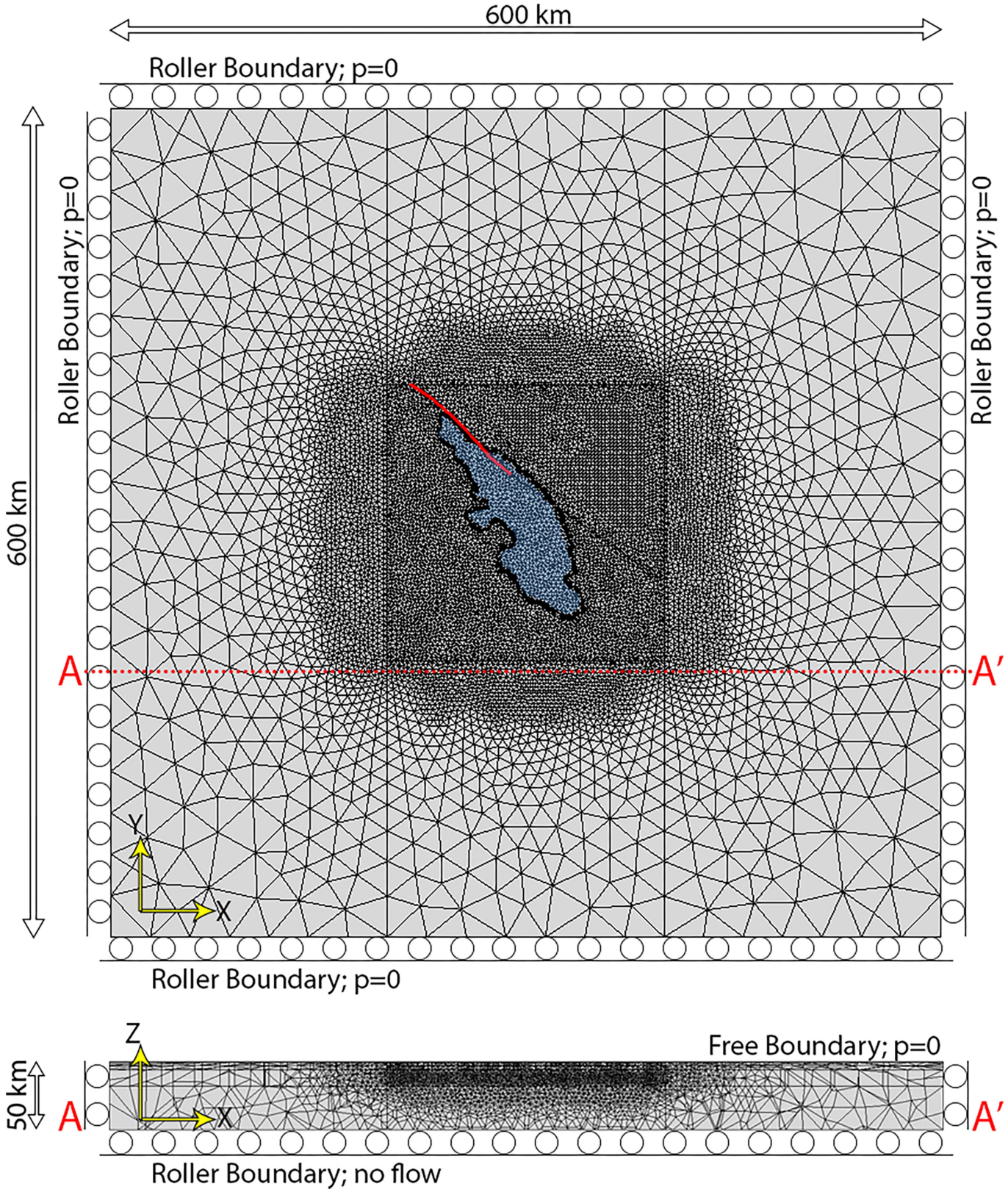

Extended Data Fig. 2 | Numerical domain. 3D finite-element method model domain. The model mesh contains about 2 million tetrahedron elements. The light blue colour represents the extent of ancient Lake Cahuilla. The prescribed vertical load is hydrostatic, to the lake maximum water head (97.2 m). The solid red line is the SSAF fault trace. The fault zone is modelled as a slab dipping to the northeast at 60° (ref. 54), with the assumed thickness of 200 m (refs. 19,46,84).

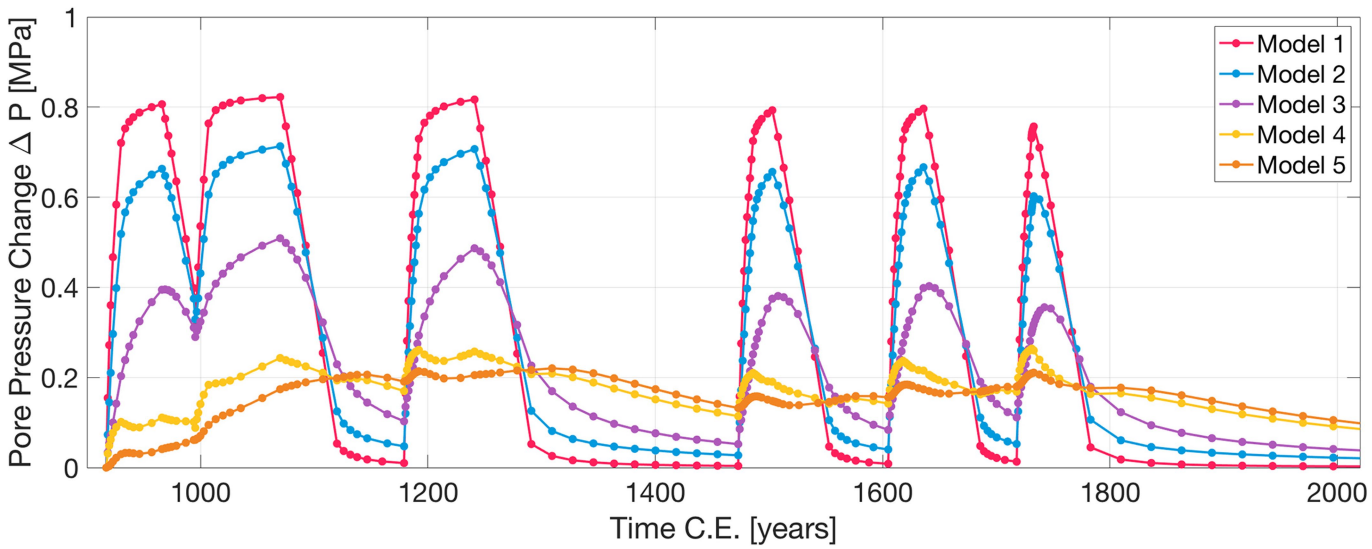

Extended Data Fig. 3 | Pore-pressure effects of lake loading. Pore pressure (MPa) on the SSAF as a function of time (year CE) at 7 km depth for location 21, a point on the fault near the centre of the lake (see Supplementary Fig. 5). Each model is based on the variable fault permeability, with model 1 as the most permeable and model 5 as the no damage zone (Extended Data Table 2).

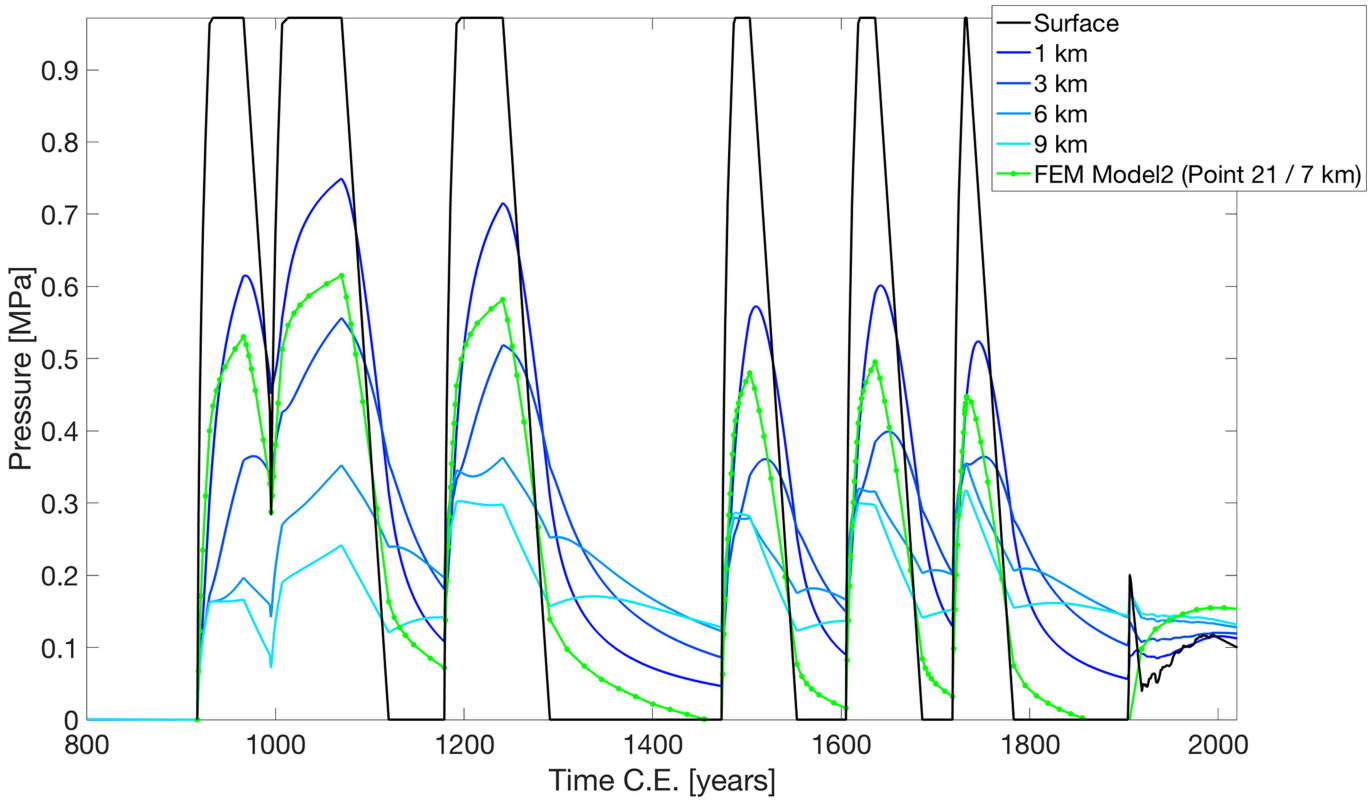

Extended Data Fig. 4 | Analytic solution for periodic loading of a poroelastic half-space. 1D analytical model of pore pressure for a variety of different depths (blue) with surface lake-level pore pressure (black). The smaller surface profile from 1905 to the present is the Salton Sea[2]. Finite-element method model 2 at 7.2 km depth (green line) shows the effect of 3D diffusion with a high-permeability fault damage zone embedded in a lower-permeability host rock. The finite-element method model at 7.2 km resembles pore pressure in the 1D analytical case at 1 km, demonstrating how a fault damage zone can transmit pore pressure to depth effectively. $\gamma = 0.1685$; $k_{\text{fault}} = 1e^{-15}$ (m^2); $k_{\text{host/1Dmodel}} = 1e^{-18}$ (m^2).

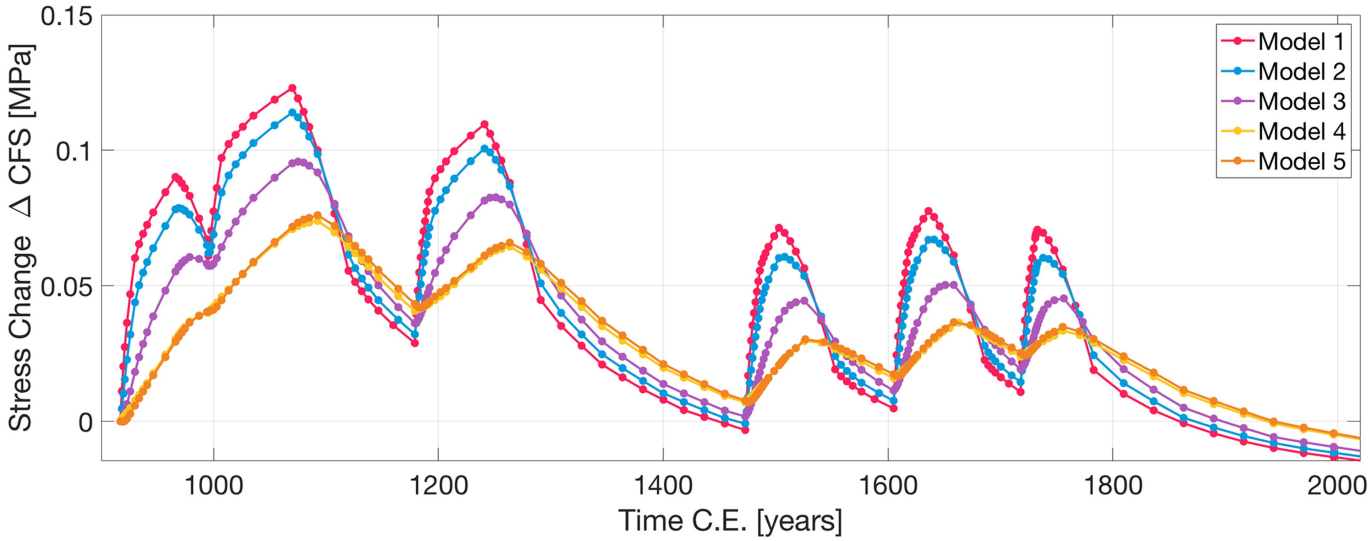

Extended Data Fig. 5 | Stress effects of lake loading. Similar to Fig. 4a but for a point farther away from the lake centre (point 24 in Supplementary Fig. 5).

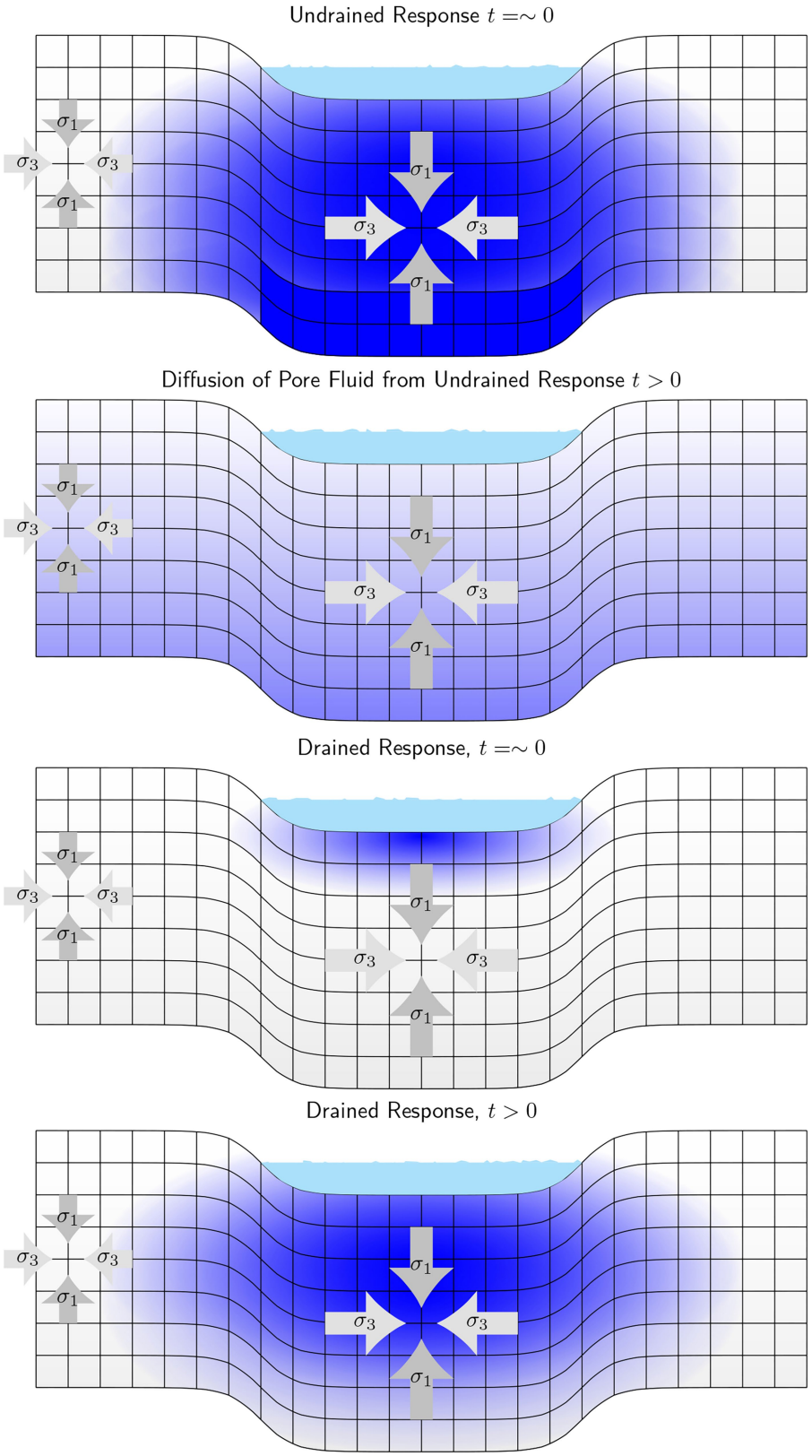

Extended Data Fig. 6 | Conceptual model of the undrained and drained effects from a lake load. The instantaneous and transient effects of the undrained and drained effects. At $t = 0$, the undrained effect is felt almost instantaneously throughout the poroelastic medium beneath the lake. As time progresses, this effect attempts to equilibrate at depth. At $t = 0$, the drained effect is not felt except for the surface poroelastic medium and the bottom of the lake. As time progresses, this effect increases pore pressure as diffusion drives fluid from the surface down. Furthermore, as the lake load is applied, areas of compression form immediately beneath the lake, whereas areas of extension are formed near the edges.

Extended Data Table 1 | Earthquake dates

Earthquake	Year	95% Confidence Range
Coa-1	1730	1721-1731
Coa-2	1610	1586-1636
Coa-3/4	1480	1459-1503
Coa-5	1200	1165-1244
Coa-6	1020	995-1040
Coa-7	970	923-1022
Coa-8	930	905-961

Best estimates (to the nearest decade) and 95% confidence ranges of earthquake dates from the OxCal model.

Extended Data Table 2 | Material properties

Hydrostratigraphy Unit	Post Brawley / Brawley	Palm Springs / Borrego	Imperial	Crystalline Basement	Mantle*	Fault Zone
Depth Range [km]	0-0.5	0.5-3	3-7	7-18	18-50	0-18
Poisson's Ratio	0.25	0.25	0.25	0.25	0.36	0.25
Young's Modulus [GPa]	50	50	50	58.4	140	1/2 host rock
Permeability [m^2]	$2{\cdot}10^{-13}$	$1.2{\cdot}10^{-12}$	$9{\cdot}10^{-14}$	10^{-18}	/	10^{-14},10^{-15},10^{-16},10^{-17}
Bulk Modulus of Solid Grains [GPa]	33	33	33	39	/	host rock
Reference	(74)	(74)	(74)	(76)	(91)	(18,54)

*The mantle is modelled as a simple linear viscoelastic material with 3×10^{19} Pa s viscosity[29]. Bulk modulus of permeating fluid (water) is assumed to equal 2.2×10^{9} Pa. Several simulations were performed to evaluate the model sensitivity to the assumed parameters. Models 1–4 considered the effect of fault-zone permeability for the assumed permeability values 10^{-14}, 10^{-15}, 10^{-16} and 10^{-17} m^2, respectively. Model 5 corresponds to a case of no damage zone (permeability and Young's modulus are the same as those of the host rock). Model 2a uses the same material properties as model 2 but assumes a spatially variable surface load controlled by a local bathymetry.